

Solar-wind predictions for the Parker Solar Probe orbit

Near-Sun extrapolations derived from an empirical solar-wind model based on Helios and OMNI observations

M. S. Venzmer and V. Bothmer

University of Goettingen, Institute for Astrophysics, Friedrich-Hund-Platz 1, 37077 Göttingen, Germany

Received 25 August 2017 / Accepted 10 November 2017

ABSTRACT

Context. The Parker Solar Probe (PSP; formerly Solar Probe Plus) mission will be humanity's first in situ exploration of the solar corona with closest perihelia at 9.86 solar radii (R_{\odot}) distance to the Sun. It will help answer hitherto unresolved questions on the heating of the solar corona and the source and acceleration of the solar wind and solar energetic particles. The scope of this study is to model the solar-wind environment for PSP's unprecedented distances in its prime mission phase during the years 2018–2025. The study is performed within the Coronagraphic German And US SolarProbePlus Survey (CGAUSS) which is the German contribution to the PSP mission as part of the Wide-field Imager for Solar Probe (WISPR).

Aims. We present an empirical solar-wind model for the inner heliosphere which is derived from OMNI and Helios data. The German-US space probes Helios 1 and Helios 2 flew in the 1970s and observed solar wind in the ecliptic within heliocentric distances of 0.29–0.98 au. The OMNI database consists of multi-spacecraft intercalibrated in situ data obtained near 1 au over more than five solar cycles. The international sunspot number (SSN) and its predictions are used to derive dependencies of the major solar-wind parameters on solar activity and to forecast their properties for the PSP mission.

Methods. The frequency distributions for the solar-wind key parameters, magnetic field strength, proton velocity, density, and temperature, are represented by lognormal functions. In addition, we consider the velocity distribution's bi-component shape, consisting of a slower and a faster part. Functional relations to solar activity are compiled with use of the OMNI data by correlating and fitting the frequency distributions with the SSN. Further, based on the combined data set from both Helios probes, the parameters' frequency distributions are fitted with respect to solar distance to obtain power law dependencies. Thus an empirical solar-wind model for the inner heliosphere confined to the ecliptic region is derived, accounting for solar activity and for solar distance through adequate shifts of the lognormal distributions. Finally, the inclusion of SSN predictions and the extrapolation down to PSP's perihelion region enables us to estimate the solar-wind environment for PSP's planned trajectory during its mission duration.

Results. The CGAUSS empirical solar-wind model for PSP yields dependencies on solar activity and solar distance for the solar-wind parameters' frequency distributions. The estimated solar-wind median values for PSP's first perihelion in 2018 at a solar distance of 0.16 au are 87 nT, 340 km s^{-1} , 214 cm^{-3} and $503\,000 \text{ K}$. The estimates for PSP's first closest perihelion, occurring in 2024 at 0.046 au ($9.86 R_{\odot}$), are 943 nT, 290 km s^{-1} , 2951 cm^{-3} , and $1930\,000 \text{ K}$. Since the modeled velocity and temperature values below approximately $20 R_{\odot}$ appear overestimated in comparison with existing observations, this suggests that PSP will directly measure solar-wind acceleration and heating processes below $20 R_{\odot}$ as planned.

Key words. solar wind – Sun: corona – Sun: heliosphere

1. Introduction

From observations of cometary tail fluctuations, Biermann (1951) inferred the presence of a continuous flow of particles from the Sun. With his theoretical solar-wind model, Parker (1958) formulated the existence of the solar wind even before the first satellites measured it in situ in 1959 (Gringauz et al. 1960; Neugebauer & Snyder 1966). The idea of a space mission flying through the solar corona dates back to the founding year of NASA in 1958 (McComas et al. 2008). Since then several space missions have measured the solar wind in situ at a wide range of heliocentric distances. In the case of Voyager 1, this was as far away as 140 au¹ in October 2017, having crossed the heliopause into interstellar space at a distance of 121 au (Gurnett et al. 2013). Various spacecraft have provided a wealth of solar-wind measurements near Earth's orbit, with WIND (Lepping et al. 1995; Ogilvie et al. 1995), SOHO (Domingo et al. 1995), ACE

(Stone et al. 1998) and DSCOVR (Burt & Smith 2012) currently providing observations while orbiting around the L1 point 1.5 million km ahead of Earth in the sunward direction. Additional measurements at other solar distances were provided by planetary missions to Venus and Mercury, such as PVO (Colin 1980) or MESSENGER (Belcher et al. 1991). Ulysses was the first probe that orbited the Sun out of the ecliptic plane and thus could measure solar wind even at polar latitudes (McComas et al. 1998). The in situ solar-wind measurements closest to the Sun to date were made by the Helios missions. Helios 1, launched in 1974, reached distances of 0.31 au. Helios 2, launched two years later, approached the Sun as close as 0.29 au (Rosenbauer et al. 1977). The NASA Parker Solar Probe² (PSP), formerly Solar Probe Plus, six years after its planned launch date in mid 2018, will reach its closest perihelia at a distance of 9.86 solar radii (R_{\odot}), that is, 0.0459 au

17
18
19
20
21
22
23
24
25
26
27
28
29
30
31
32

¹ <https://voyager.jpl.nasa.gov/>

² <http://parkersolarprobe.jhuapl.edu/>

1 (Fox et al. 2015). This distance will be achieved through seven
 2 Venus gravity assists with orbital periods of 88–168 days. In its
 3 prime mission time 2018–2025 PSP provides 24 orbits with per-
 4 helia inside 0.25 au (Fox et al. 2015). Even its first perihelion,
 5 93 days after launch in 2018, will take PSP to an unprecedented
 6 distance of 0.16 au ($35.7 R_{\odot}$). In comparison, the ESA Solar
 7 Orbiter mission with a planned launch in February 2019 will
 8 have its closest perihelia at 0.28 au (Müller et al. 2013).

9 The key PSP science objectives are to “trace the flow of en-
 10 ergy that heats and accelerates the solar corona and solar wind,
 11 determine the structure and dynamics of the plasma and mag-
 12 netic fields at the sources of the solar wind, and explore mecha-
 13 nisms that accelerate and transport energetic particles” as stated
 14 in Fox et al. (2015). To achieve these goals, PSP has four sci-
 15 entific instruments on board: FIELDS for the measurement of
 16 magnetic fields and AC/DC electric fields (Bale et al. 2016),
 17 SWEAP for the measurement of flux of electrons, protons and
 18 alphas (Kasper et al. 2016), ISOIS for the measurement of so-
 19 lar energetic particles (SEPs; McComas et al. 2016) and WISPR
 20 for the measurement of coronal and inner heliospheric structures
 21 (Vourlidas et al. 2016).

22 The study presented in this paper is undertaken in the Coro-
 23 nagraphic German And US SolarProbePlus Survey (CGAUSS)
 24 project, which is the German contribution to the PSP mission as
 25 part of the Wide-field Imager for Solar PRobe (WISPR). WISPR
 26 will contribute to the PSP science goals by deriving the three-
 27 dimensional structure of the solar corona through which the in
 28 situ measurements are made to determine the sources of the
 29 solar wind. It will provide density power spectra over a wide
 30 range of structures (e.g., streamers, pseudostreamers and equa-
 31 torial coronal holes) for determining the roles of turbulence,
 32 waves, and pressure-balanced structures in the solar wind. It will
 33 also measure the physical properties, such as speed and density
 34 jumps of SEP-producing shocks and their coronal mass ejection
 35 (CME) drivers as they evolve in the corona and inner heliosphere
 36 (Vourlidas et al. 2016). In order to help optimize the WISPR and
 37 PSP preplanning of the science operations, knowledge of the ex-
 38 pected solar-wind environment is needed. For this purpose the
 39 solar-wind environment is extrapolated down to the closest peri-
 40 helion of $9.86 R_{\odot}$ distance to the Sun using in situ solar-wind data
 41 from the Helios probes and near 1 au data from various satellites
 42 compiled in the OMNI solar-wind database.

43 Generally, two types of solar wind are observed in the
 44 heliosphere – slow and fast streams (Neugebauer & Snyder
 45 1966; Schwenn 1983). Slow solar wind has typical speeds
 46 of $<400 \text{ km s}^{-1}$ and fast solar wind has speeds $>600 \text{ km s}^{-1}$
 47 (Schwenn 1990, p. 144). Their different compositions and char-
 48 acteristics indicate different sources and generation processes
 49 (McGregor et al. 2011b). Fast streams are found to originate
 50 from coronal holes as confirmed by Ulysses’ out-of-ecliptic
 51 measurements (McComas et al. 1998). The source of slow wind,
 52 and its eventually different types (Schwenn 1983), is still a
 53 subject of controversial discussions because several scenarios
 54 are possible to explain its origin from closed magnetic struc-
 55 tures in the solar corona, such as intermittent reconnection at
 56 the top of helmet streamers and from coronal hole boundaries
 57 (Kilpua et al. 2016). The occurrence frequency of these slow and
 58 fast streams varies strongly with solar activity and their inter-
 59 actions lead to phenomena such as stream interaction regions
 60 which may persist for many solar rotations (“co-rotating” inter-
 61 action regions) if the coronal source regions are quasi-stationary
 62 (Balogh et al. 1999). Embedded in the slow and fast solar-wind
 63 streams are transient flows of CMEs – the faster ones driving
 64 shock waves ahead (Gosling et al. 1974). Their rate follows the

solar activity cycle and varies in near 1 au measurements be-
 65 between only one CME every couple of days during solar cy-
 66 cle minima up to multiple CMEs observed over several days
 67 at times of solar maxima, that is, the CME-associated flow
 68 share of the solar wind raises from about 5% up to about 50%
 69 (Richardson & Cane 2012).

70 It is not known which specific solar-wind type or structure
 71 PSP will encounter at a given time during its mission, there-
 72 fore we extrapolate the probability distributions of the major
 73 solar-wind parameters from existing solar-wind measurements
 74 and take solar cycle dependencies into account. As a baseline
 75 we describe the solar-wind environment through the key quanti-
 76 ties of a magnetized plasma: magnetic field strength, density and
 77 temperature. Furthermore, the bulk flow velocity is the defining
 78 parameter of the two types of solar wind. Solar-wind quantities,
 79 like flux densities, mass flux, and plasma beta, can be directly
 80 derived from these four parameters. In the analyses, we treat the
 81 solar wind as a proton plasma – the average helium abundance
 82 is about 4.5% and in slow wind at solar cycle minimum is even
 83 less than 2% (Feldman et al. 1978; Schwenn 1983; Kasper et al.
 84 2012).

85 Our approach is to obtain analytical representations of the
 86 shapes of the solar-wind parameter’s frequency distributions in
 87 Sect. 2, of their solar activity dependence in Sect. 3 and of their
 88 solar distance scaling in Sect. 4. The solar-wind parameters’ fre-
 89 quency distributions and solar activity dependence is derived
 90 from near-Earth solar wind and sunspot number (SSN) time se-
 91 ries with a duration of almost five solar cycles. Their distance de-
 92 pendence is derived from Helios solar-wind measurements cov-
 93 ering more than two thirds of the distance to the Sun and more
 94 than half a solar cycle. From a combination of the obtained fre-
 95 quency distributions, SSN dependence functions, and solar dis-
 96 tance dependence functions, a general solar-wind model is built
 97 in Sect. 5, representing the solar activity and distance behavior.
 98 Finally, this empirical model is fed with SSN predictions and
 99 extrapolated to PSP’s planned orbital positions in Sect. 6.

2. Frequency distributions of the solar-wind parameters

100 The solar-wind parameters are highly variable due to short-term
 101 variations from structures such as slow and fast wind streams, in-
 102 teraction regions, and CMEs, whose rate and properties depend
 103 on the phase of the solar activity cycle. Hence, for deriving char-
 104 acteristic frequency distributions for the solar-wind parameters,
 105 measurements over long-term time spans are needed. The abun-
 106 dance of the near-Earth hourly OMNI data set is ideally suited
 107 for this purpose, because to date it spans almost five solar cycles.

108 The OMNI 2 data set (King & Papitashvili 2005) combines
 109 solar-wind magnetic field and plasma data collected by var-
 110 ious satellites since 1963, currently by WIND and by ACE.
 111 This intercalibrated multi-spacecraft data is time-shifted to the
 112 nose of the Earth’s bow shock. The data is obtained from the
 113 OMNIWeb interface³ at NASA’s Space Physics Data Facility
 114 (SPDF), Goddard Space Flight Center (GSFC). In this study
 115 the whole hourly data until 31 December 2016 is used, start-
 116 ing from 27 November 1963 (for the temperature from 26 July
 117 1965). The data coverage of the different parameters is in the
 118 range 67–74%, corresponding to a total duration of 36–40 yrs.
 119 We note that a test-comparison of hourly averaged data with
 120 higher-time-resolution data for the available shorter time span
 121 1981–2016 did not show significant differences in our results.

122 ³ <http://omniweb.gsfc.nasa.gov/>

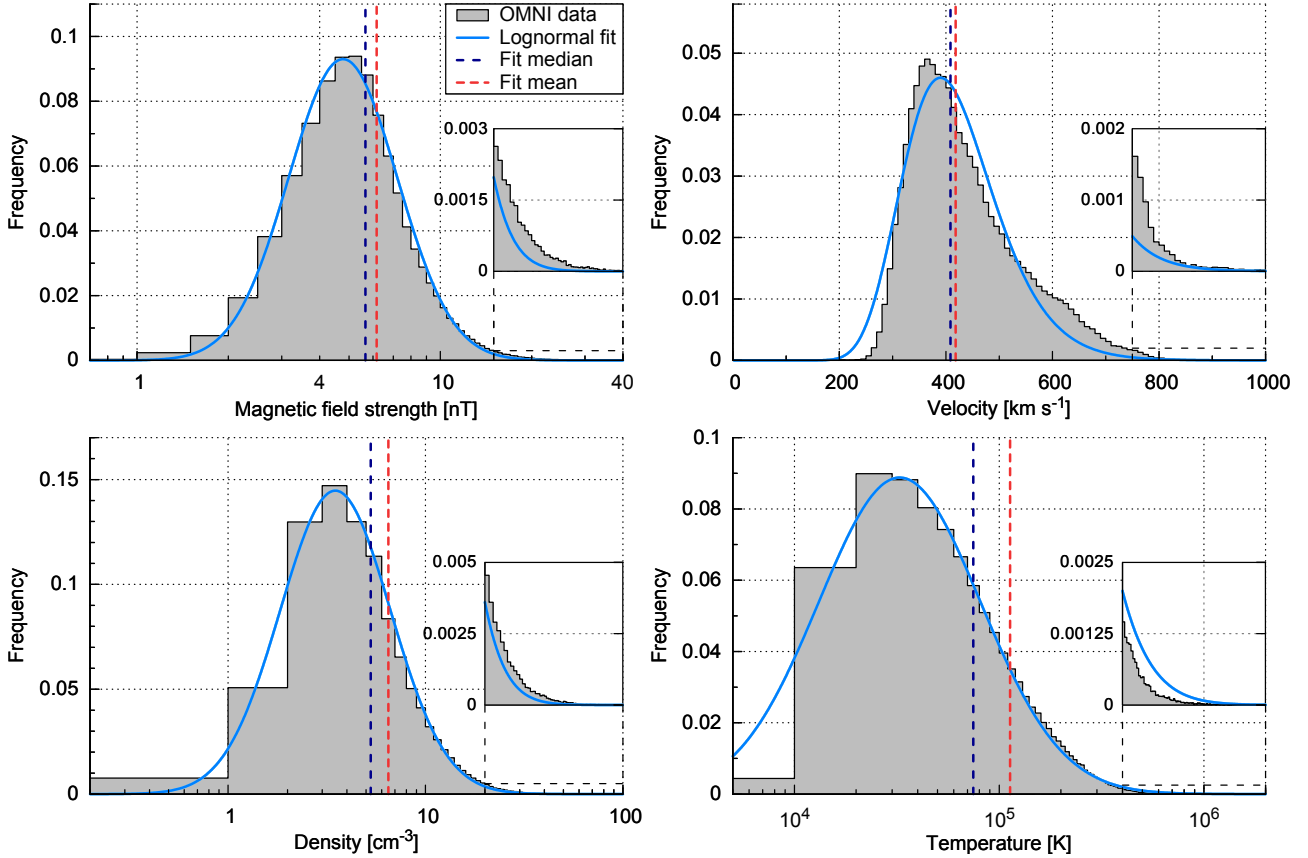


Fig. 1. Frequency distributions of the four solar-wind parameters and their lognormal fits derived from the hourly OMNI data set. The histograms have bins of 0.5 nT, 10 km s⁻¹, 1 cm⁻³ and 10 000 K. The fits' median and mean values are indicated as well. The *insets* show zoomed-in views of the high-value tails of the distributions.

According to the OMNI data precision and maximal parameter ranges we specify bin sizes of 0.5 nT for the magnetic field strength, 10 km s⁻¹ for the velocity, 1 cm⁻³ for the density and 10 000 K for the temperature. The frequency distributions of the solar-wind magnetic field strength, proton velocity, density and temperature are shown in Fig. 1. The solar-wind magnetic field strength is in the range 0.4–62 nT, the velocity in the range 156–1189 km s⁻¹, the density in the range 0–117 cm⁻³, the temperature in the range 3450–6.63 × 10⁶ K, and the mean data values are at 6.28 nT, 436 km s⁻¹, 6.8 cm⁻³ and 1.05 × 10⁵ K. These ranges and mean values are as statistically expected from previous analyses of near 1 au solar-wind data (e.g., Table 3.3 in Bothmer & Daglis 2007, p. 39). Much higher or lower peak values at 1 au have been observed in extraordinary events, such as the 23 July 2012 CME with a speed of over 2000 km s⁻¹ and a peak field strength of about 100 nT that was observed by STEREO A (Russell et al. 2013), or the solar-wind disappearance event observed in May 1999 with density values even down to 0.2 cm⁻³ (Lazarus 2000).

The frequency distributions of the solar-wind parameters, magnetic field strength, proton density, and temperature, can be well approximated by lognormal distributions, whereas the proton velocity's frequency has a differing shape, as shown in Veselovsky et al. (2010). We investigate how well all four solar-wind parameters' frequency distributions can be represented by lognormal functions, which we use in the process of a least squares regression fitting. The lognormal function,

$$W(x) = \frac{1}{\sigma \sqrt{2\pi} x} \exp\left(-\frac{(\ln x - \mu)^2}{2\sigma^2}\right), \quad (1)$$

depends on the location μ and the shape parameter σ . Changes in μ affect both the horizontal and vertical scaling of the function whereas σ influences its shape. The distribution's median x_{med} and mean x_{avg} (average) positions are easily interpreted and are directly calculated from μ and σ :

$$x_{\text{med}} = \exp(\mu) \quad \Longleftrightarrow \quad \mu = \ln(x_{\text{med}}), \quad (2)$$

$$x_{\text{avg}} = \exp\left(\mu + \frac{\sigma^2}{2}\right) \quad \Longleftrightarrow \quad \sigma = \sqrt{2 \ln\left(\frac{x_{\text{avg}}}{x_{\text{med}}}\right)}. \quad (3)$$

It is apparent that the mean is always larger than the median. Replacing the variables μ and σ with these relations, the lognormal function (1) becomes

$$W(x) = \frac{1}{2 \sqrt{\pi \ln\left(\frac{x_{\text{avg}}}{x_{\text{med}}}\right)} x} \exp\left(-\frac{\ln^2\left(\frac{x}{x_{\text{med}}}\right)}{4 \ln\left(\frac{x_{\text{avg}}}{x_{\text{med}}}\right)}\right). \quad (4)$$

The values of x_{med} and x_{avg} obtained from fitting the individual solar-wind frequency distributions are listed in Table 1.

From visual inspection, the resulting fit curves describe the shape of the magnetic field strength, the density and the temperature distributions well, as can be seen in Fig. 1. However, for the velocity, the fit function appears not to be as good in describing the measured distribution's more complex shape around its peak and in the higher velocity range. This also can be inferred from the sum of absolute residuals (SAR) between data and fit, listed in Table 1 as a percentage of the distribution area, being almost three times larger than those from the other parameters. In order to find a better fit result for the velocity distribution, we

Table 1. Resulting fit coefficients from the fitting of the lognormal function (4) to the shape of the solar-wind parameters' frequency distributions from near 1 au OMNI hourly data.

Parameter	Median x_{med}	Mean x_{avg}	Balance c	SAR [%]
Magnetic field [nT]	5.661(16)	6.164(18)	–	6.83
Velocity [10^2 km s^{-1}]	4.085(19)	4.183(20)	–	18.69
Density [cm^{-3}]	5.276(24)	6.484(34)	–	6.48
Temperature [10^4 K]	7.470(17)	11.301(32)	–	5.78
Velocity [10^2 km s^{-1}]	W_1 3.68(20) W_2	4.89(14) 3.72(20) W_{II}	5.00(14) 4.42(14) ^a	0.504(62) – 4.20

Notes. For the velocity, the fit parameters of the double lognormal function (5) are also listed, as well as the median and mean values of the resulting velocity fit. The numbers in parentheses are the errors on the corresponding last digits of the quoted value. They are calculated from the estimated standard deviations of the fit parameters. For each parameter, the sum of absolute residuals between data and fit (in percentage of the distribution area) is also listed. ^(a) Error estimates derived from the individual fit part errors.

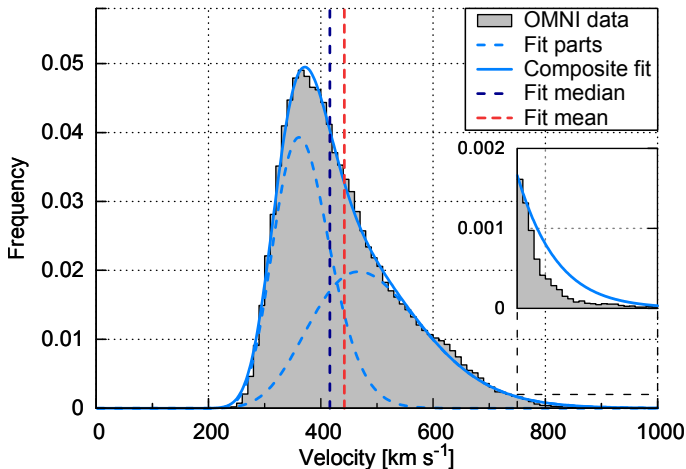


Fig. 2. Velocity frequency distribution (same as in Fig. 1) and its compositional lognormal fit. The fit's median and mean values and its two fit parts are indicated as well. The inset is a zoomed-in view of the high value tail of the distribution.

assume that the velocity distribution can be made up of at least two overlapping branches (McGregor et al. 2011a). Therefore a compositional approach is chosen by combining two lognormal functions (4), involving more fit variables:

$$W_{\text{II}}(x) = c \cdot W_1(x) + (1 - c) \cdot W_2(x). \quad (5)$$

The balancing parameter c ensures that the resulting function remains normalized as it represents a probability distribution. The fitting of $W_{\text{II}}(x)$ to the velocity's frequency distribution yields the values of the now five fit parameters (c , $x_{\text{med},1}$, $x_{\text{avg},1}$, $x_{\text{med},2}$ and $x_{\text{avg},2}$) as listed in Table 1 together with the median and mean values of the composed distribution, which can be derived by solving

$$\int W_{\text{II}}(x) dx = 0 \quad \text{and} \quad \int x W_{\text{II}}(x) dx = 0. \quad (6)$$

This more complex fit function is more accurate in describing the velocity's frequency distribution as shown in Fig. 2. Thus in the following Sections we keep the double lognormal ansatz for all velocity frequency fits.

For the bulk of the solar wind these static lognormal functions describe the parameters' distributions well. The abnormally high parameter values in the distribution functions can be

attributed to shock/CME events in agreement with the results of the OMNI solar-wind investigations by Richardson & Cane (2012). The simple lognormal fit functions underestimate the frequencies in their high-value tails, except for the temperature's tail which is overestimated, as seen in the insets of Fig. 1. This appears to be because CMEs do not come with abnormally high temperatures, but rather with temperatures lower than those of the average solar wind (Forsyth et al. 2006). The velocity's compositional lognormal fit only slightly overestimates its tail as seen in the inset of Fig. 2. The slow and fast part contribute almost equally ($c \approx 0.5$) to the long-term velocity distribution function.

3. Solar activity dependence of the solar-wind frequency distributions

In the next step we investigate how the long-term solar-wind distribution functions presented in the previous section depend on general solar activity. Therefore we examine their correlation with the SSN, being a commonly used long-term solar activity index, and determine the time lags with the highest correlation coefficients.

For the correlations we fit lognormal functions to the frequency distributions as in Sect. 2, but implement linear relations to the yearly SSN, allowing shifting of the distribution functions with SSN. For the velocity the approach is different insofar as its two components are kept fixed and instead their balance is modified with the changing SSN. Thus we obtain solar-activity-dependent models for the frequency distributions of all four solar-wind parameters.

The international sunspot number (1963–2016) is provided by the online catalog⁴ at the World Data Center – Sunspot Index and Long-term Solar Observations (WDC-SILSO), Solar Influences Data Analysis Center (SIDC), Royal Observatory of Belgium (ROB).

Yearly medians of the solar-wind parameters and the yearly SSN together with the solar cycle number are shown in the upper part of Fig. 3. The reason for correlating the SSN to the solar-wind median values is because the position of a lognormal function is defined by its median. The data are averaged to yearly values to avoid seasonal effects during the Earth's orbit around the Sun caused by its variations in solar latitude and distance. The solar-wind velocity, density, and temperature depend

⁴ <http://www.sidc.be/silso/>

Table 2. Resulting fit coefficients from the OMNI data, based on the linear SSN dependencies (7) and (8).

Parameter	Median		Mean scaling factor a_{avg}	Balance		SSN lag [years]
	SSN factor a_{med}	baseline b_{med}		SSN factor c_a	baseline c_b	
Magnetic field [nT]	$1.309(19) \times 10^{-2}$	4.285(17)	$8.786(78) \times 10^{-2}$	–	–	0
Density [cm^{-3}]	$3.81(25) \times 10^{-3}$	4.495(26)	$3.050(27) \times 10^{-1}$	–	–	6
Temperature [10^4 K]	$1.974(26) \times 10^{-2}$	5.729(19)	$6.541(28) \times 10^{-1}$	–	–	3
Velocity W'_1 [10^2 km s^{-1}]	–	3.633(12)	$1.008(37) \times 10^{-2}$	$-1.799(95) \times 10^{-3}$	0.638(32)	3
Velocity W'_2 [10^2 km s^{-1}]	–	4.831(81)	2.31(20)	$\times 10^{-2}$		

Notes. For the velocity the fit parameters from the double lognormal fit (5) and their balancing function (9) are given. The numbers in parentheses are the errors on the corresponding last digits of the quoted value. They are calculated from the estimated standard deviations of the fit parameters. The listed SSN time lags are used for the fits.

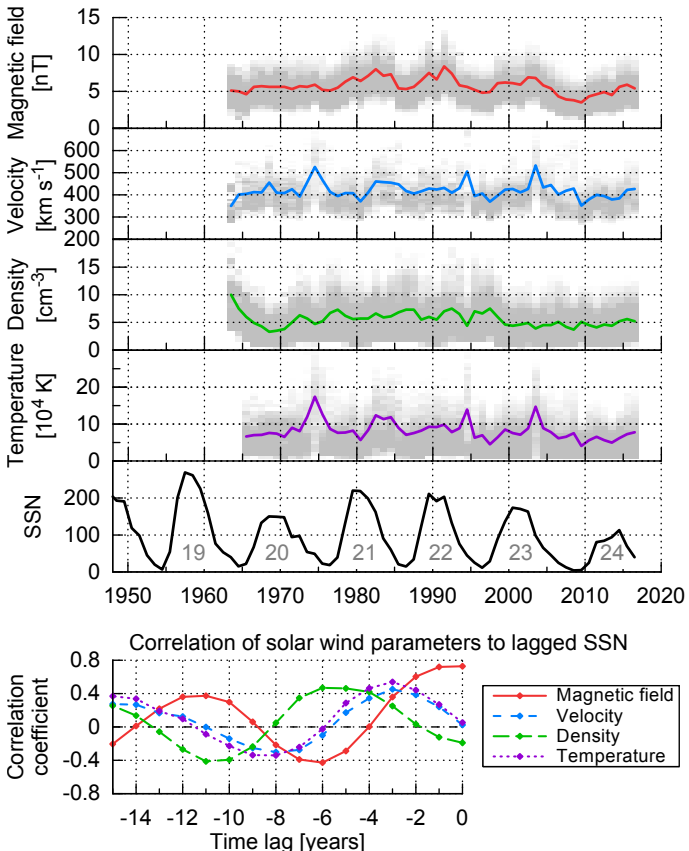


Fig. 3. Solar-wind parameter yearly frequencies (gray shading) with yearly medians (lines) derived from OMNI data and the yearly SSN from the SILSO World Data Center (1963–2016) with solar cycle number (top). Their correlation coefficients with the yearly SSN are calculated for time lags back to –15 yrs (bottom).

on the state of the solar cycle (Schwenn 1983). For instance the fast solar wind occurs at times when polar coronal holes extend to lower latitudes, a typical feature of the declining phase of the solar cycle as pointed out by Bothmer & Daglis (2007, p. 75, Fig. 3.52). Therefore the solar-wind velocity, density, and temperature maxima exhibit time lags relative to the SSN maxima.

The correlation coefficients of the solar wind parameters with the yearly SSN shown in the bottom part of Fig. 3 are calculated for time lags back to –15 yrs to cover a time span longer than a solar cycle. As expected, the amplitudes of the variations in the correlations of all parameters decline with increasing time lag and show a period of about 11 years. The highest correlation coefficient of 0.728 to the SSN is found for the magnetic field

strength; it has no time lag. This finding is anticipated because the SSN is found to be directly proportional to the evolution of the photospheric magnetic flux (Smith & Balogh 2003). Velocity and temperature show time lags of 3 years with peak correlation coefficients of 0.453 and 0.540. The density with a correlation coefficient of 0.468 has a time lag of 6 years, which is in agreement with the density anticorrelation to the SSN reported by Bougeret et al. (1984).

Next we create solar-activity-dependent analytical representations of the solar wind frequency distributions. This is achieved by shifting the median positions of the lognormal distributions as a linear function of the SSN. To enable these shifts, we add a linear SSN dependency to the median,

$$x_{\text{med}}(\text{ssn}) = a_{\text{med}} \cdot \text{ssn} + b_{\text{med}}, \quad (7)$$

using a factor to the SSN a_{med} with a baseline b_{med} . We relate the mean with a scaling factor to the median to transfer its SSN dependency:

$$x_{\text{avg}}(\text{ssn}) = (1 + a_{\text{avg}}) \cdot x_{\text{med}}(\text{ssn}). \quad (8)$$

These relations, substituted into the lognormal function (4), lead to a new SSN-dependent function $W'(x, \text{ssn})$. This function is then fitted to the yearly data, using the yearly SSN as input parameter. The SSN is offset with the individual time lags determined before for each parameter, to benefit from the higher correlation. The values of the three resulting fit coefficients (a_{med} , b_{med} and a_{avg}) are presented in Table 2.

Naturally, the fit models match with the general data trends, as can be seen from Fig. 4, though single year variations are not replicated by the model (e.g., the high velocity and temperature values in 1974, 1994, and 2003). The comparison of this model with the yearly data median values with respect to the lagged SSN shows that the medians obtained from the modeling have a similar slope, as shown in Fig. 5.

Again, the solar-wind velocity needs a special treatment because of the application of the double lognormal distribution (5). Since it is well known that slow and fast solar-wind stream occurrence rates follow the solar cycle, we keep the two velocity components' positions SSN-independent ($x_{\text{med}} = b_{\text{med}}$) and vary instead their balance with the SSN:

$$c(\text{ssn}) = c_a \cdot \text{ssn} + c_b. \quad (9)$$

The fit result (see Table 2) yields a model in which three years after solar cycle minimum (SSN of zero) the contribution of slow solar wind to the overall solar wind distribution reaches a maximum value (about 64%) and decreases with increasing SSN as shown in Fig. 6.

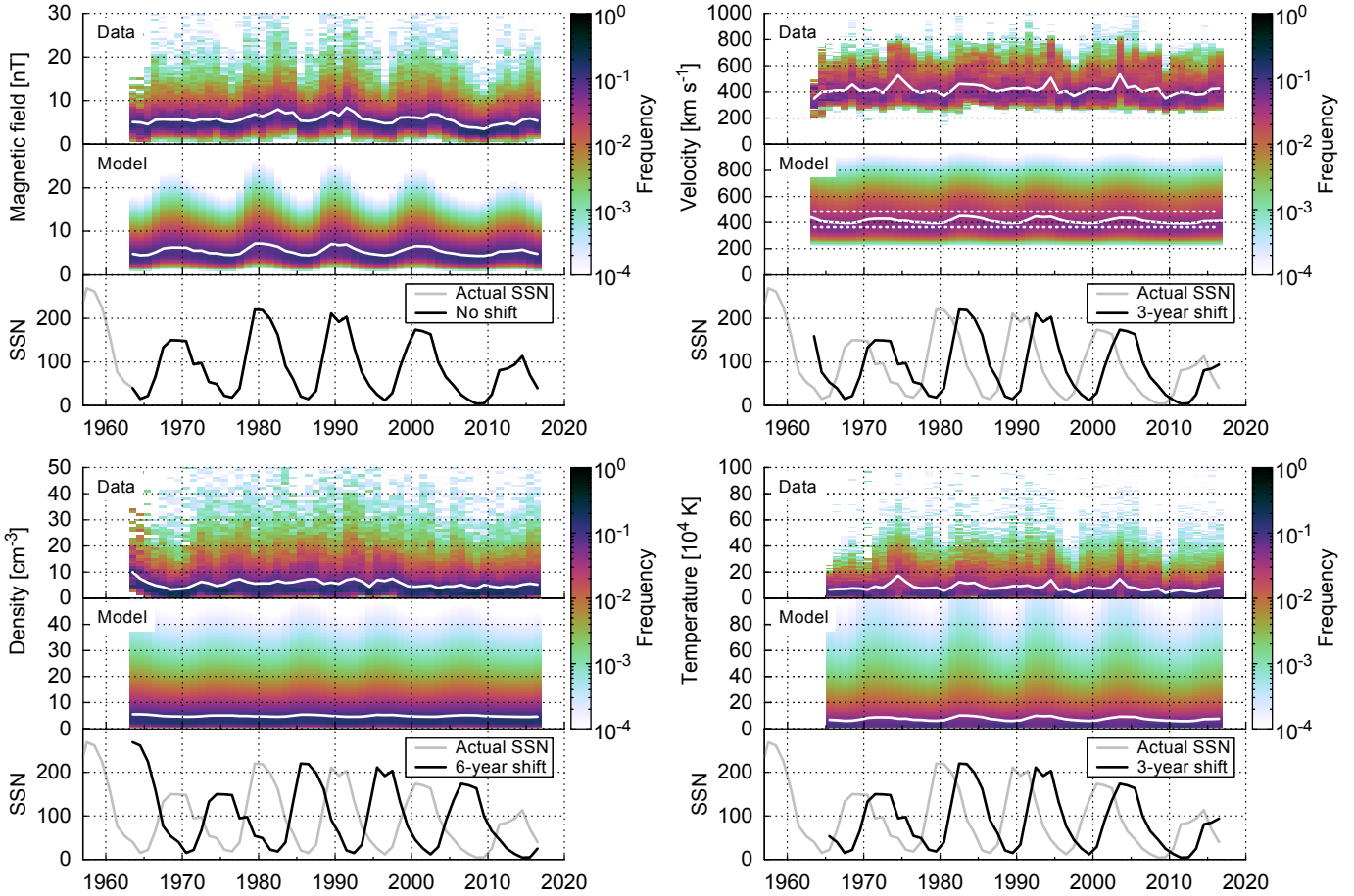


Fig. 4. Solar wind parameter yearly data frequencies and lognormal fit models, both with their median values (white lines) over the OMNI time period 1963–2016. The corresponding yearly SSN and the shifted SSN for the models are indicated by gray and black lines. The velocity median is derived from the SSN-weighted constant lognormal parts (dotted lines).

To investigate the amount of slow and fast wind contributions depending on solar activity, we apply the commonly used constant velocity threshold of $v_{\text{th}} = 400 \text{ km s}^{-1}$ (Schwenn 1990, p. 144). The linear fit to the yearly data ratio and the derived model ratio show a good agreement (see Fig. 6). The to-some-degree steeper balance parameter of the double fit function used in this model cannot be compared directly with specific velocity thresholds between slow and fast solar wind. However, it appears to be a more realistic approach than just taking a specific velocity threshold for the slow and fast wind, in agreement with the overlapping nature of the velocity flows reported by McGregor et al. (2011a).

4. Solar distance dependency

In order to derive heliocentric distance relationships of the bulk solar wind distribution functions, we apply and fit power law dependencies to the Helios data. We then examine how the fits may be extrapolated towards the Sun and in particular in to the PSP orbit. We use the fitting methods of Sect. 2 for the distance-binned combined data from both Helios probes. Helios' highly elliptical orbits in the ecliptic covered a solar distance range of 0.31–0.98 au in case of Helios 1 and 0.29–0.98 au in case of Helios 2. Launched during solar cycle minimum, the data of both probes cover the rise to the maximum of cycle 21, covering ~6.5 yrs at varying distances to the Sun.

We investigate hourly averages of the Helios data in the same way as with the OMNI data. The Helios 1 merged

hourly data from the magnetometer and plasma instruments (Rosenbauer et al. 1977) include ~12.5 orbits for the time range 10 December 1974 to 14 June 1981, and those for Helios 2 include ~8 orbits for the time span 1 January 1976 to 4 March 1980. The data are retrieved from the Coordinated Data Analysis Web (CDAWeb) interface at NASA's GSFC/SPDF⁵.

The Helios 1 magnetometer data coverage for this data set is about 43% (i.e., 2.8 yrs), and that of Helios 2 amounts to 54% (i.e., 2.3 yrs). The plasma data coverage is 76% (i.e., 5.0 yrs) in case of Helios 1 and 92% (i.e., 3.9 yrs) in case of Helios 2. Thus, using this data, we point out that its time coverage is unequally distributed over the solar cycle. Considering the data gap distributions, the amount of data during solar cycle minimum up to mid 1977, that is, the transition from minimum to maximum, covers about 68% of this period whereas during maximum of cycle 21 data are available only 38% of the time. This Helios data bias towards solar minimum is one reason why in this study the Helios solar wind data are not used to derive long-term frequency distributions and solar-cycle dependencies for the key solar wind parameters.

The radial dependencies of the key solar-wind parameters over the distance range 0.29–0.98 au measured by both Helios probes are plotted in Fig. 7, together with their median and mean values for different solar distances, calculated for the minimal distance resolution 0.01 au of the data set. Assuming a radial solar-wind outflow, it is expected that the distance

⁵ <http://spdf.gsfc.nasa.gov/>

Table 3. Fit coefficients for the median and mean solar distance dependencies (10) of the four solar wind parameters derived from the combined Helios 1 and 2 data.

Parameter	Median		Mean		Crossing distance	Yearly variation
	d_{med}	e_{med}	d_{avg}	e_{avg}	[au]	Δe
Magnetic field [nT]	5.377(92)	-1.655(17)	6.05(10)	-1.546(18)	0.339(11)	0.11
Velocity [10^2 km s^{-1}]	4.107(28)	0.058(13)	4.356(24)	0.049(10)	$0.7(83) \times 10^3$	0.012
Density [cm^{-3}]	5.61(27)	-2.093(46)	7.57(30)	-2.010(38)	0.027(73)	0.072
Temperature [10^4 K]	7.14(23)	-0.913(39)	9.67(21)	-0.792(28)	0.082(85)	0.050

Notes. The numbers in parentheses are the errors on the corresponding last digits of the quoted value. They are calculated from the estimated standard deviations of the fit parameters. The crossing distances indicate where the median and mean fits intersect each other. The yearly variation is the weighted standard deviation derived from the yearly fit exponents seen in Fig. 9.

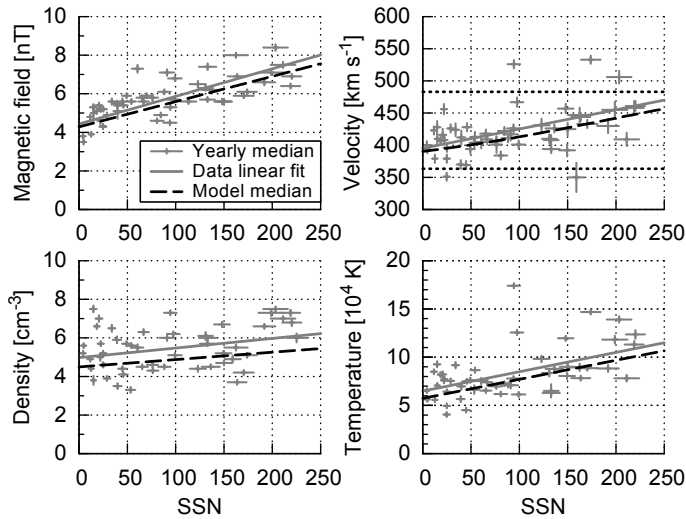


Fig. 5. Solar-wind parameter medians with respect to the lagged SSN. The yearly data medians (+) with their weighted linear fit (solid lines) are obtained from OMNI data. The error bars denote the SSN standard deviation and the relative weight from the yearly data coverage. The SSN-dependent median (dashed lines) is derived from the lognormal model fit. For the velocity the median is derived from the SSN-weighting (9) of the slow and fast model parts (dotted lines), whose magnitudes are SSN independent.

dependence of the solar-wind parameters over the Helios data range 0.29–0.98 au can be described through power law scaling. Therefore we use the power law function,

$$x(r) = d \cdot r^e, \quad (10)$$

for the regression fit of the median and mean, with r being the solar distance in astronomical units, d the magnitude at 1 au and e the exponent. The fits are weighted through the different data counts per bin. The obtained coefficients for the median and mean power law fits (d_{med} , e_{med} , d_{avg} and e_{avg}) are listed in Table 3 and their corresponding curves are shown in Fig. 7.

Our derived exponents agree with those found in existing studies from the Helios observations: Mariani et al. (1978) derived the exponents for the magnetic field strength separately for the fast and slow solar wind as $B_{\text{fast}} \propto r^{-1.54}$ and $B_{\text{slow}} \propto r^{-1.61}$, ours is $B_{\text{avg}} \propto r^{-1.55}$. The velocity exponent $v_{\text{avg}} \propto r^{0.049}$ matches with the values found by Schwenn (1983, 1990), who derived the distance dependencies for both Helios spacecraft separately as $v_{\text{H1}} \propto r^{0.083}$ and $v_{\text{H2}} \propto r^{0.036}$. The calculated density exponent $n_{\text{avg}} \propto r^{-2.01}$ agrees well with the Helios plasma density model derived by Bougeret et al. (1984) yielding $n \propto r^{-2.10}$. The temperature exponent $T_{\text{avg}} \propto r^{-0.79}$ is similar to those in the studies

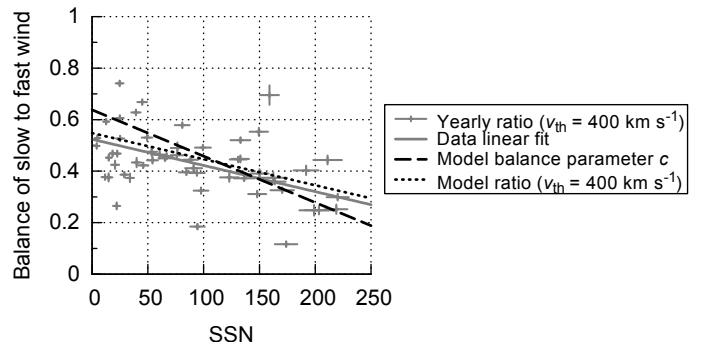


Fig. 6. Ratio of slow to fast solar wind for a SSN lagged by 3 years. The yearly ratios (+) and their weighted linear fit (solid line) are obtained from OMNI data with a threshold velocity of $v_{\text{th}} = 400 \text{ km s}^{-1}$. The error bars denote the SSN standard deviation and the relative weight from the yearly data coverage. The model's balance parameter (9) and derived ratio (same threshold) are plotted as dashed and dotted lines.

by Hellinger et al. (2011, 2013), who also derived the exponents separately for the fast and the slow solar wind: $T_{\text{fast}} \propto r^{-0.74}$ and $T_{\text{slow}} \propto r^{-0.58}$.

The mean and median velocity fit exponents acquired from the Helios data are very similar, which indicates that they can be kept identical so that the basic shape of the frequency distribution does not change with distance. Conversely, the mean and median fits for the magnetic field strength cross each other at 0.339 au (see Table 3) and the mean becomes slightly lower than the median at smaller distances. Thus, below that distance the frequency distribution can no longer be well described by a lognormal function, because the mean of a lognormal function has to be larger than its median (as pointed out in Sect. 2), that is, the location of the crossing indicates that the parameter's distribution is no longer of a lognormal shape thereafter. The fits for the proton temperature show a similar behavior, having an extrapolated intersection at 0.082 au. Therefore the extrapolation of the magnetic field and temperature distribution frequencies to the PSP orbit by applying lognormal functions is limited. The crossing points limit the regions where the distribution's shapes can still be considered lognormal.

In order to still fit and extrapolate lognormal functions with the data, we assume that the shapes can be considered lognormal at all distances. For the frequency distribution fit function to be discussed in the following paragraph, we reduce the fit exponents e_{med} and e_{avg} to only one. We note that this simplification leads to slightly larger modeling errors, especially in case of the magnetic field strength.

Next we retrieve the frequency distributions of the four solar wind parameters in solar distance bins of 0.01 au, choosing the

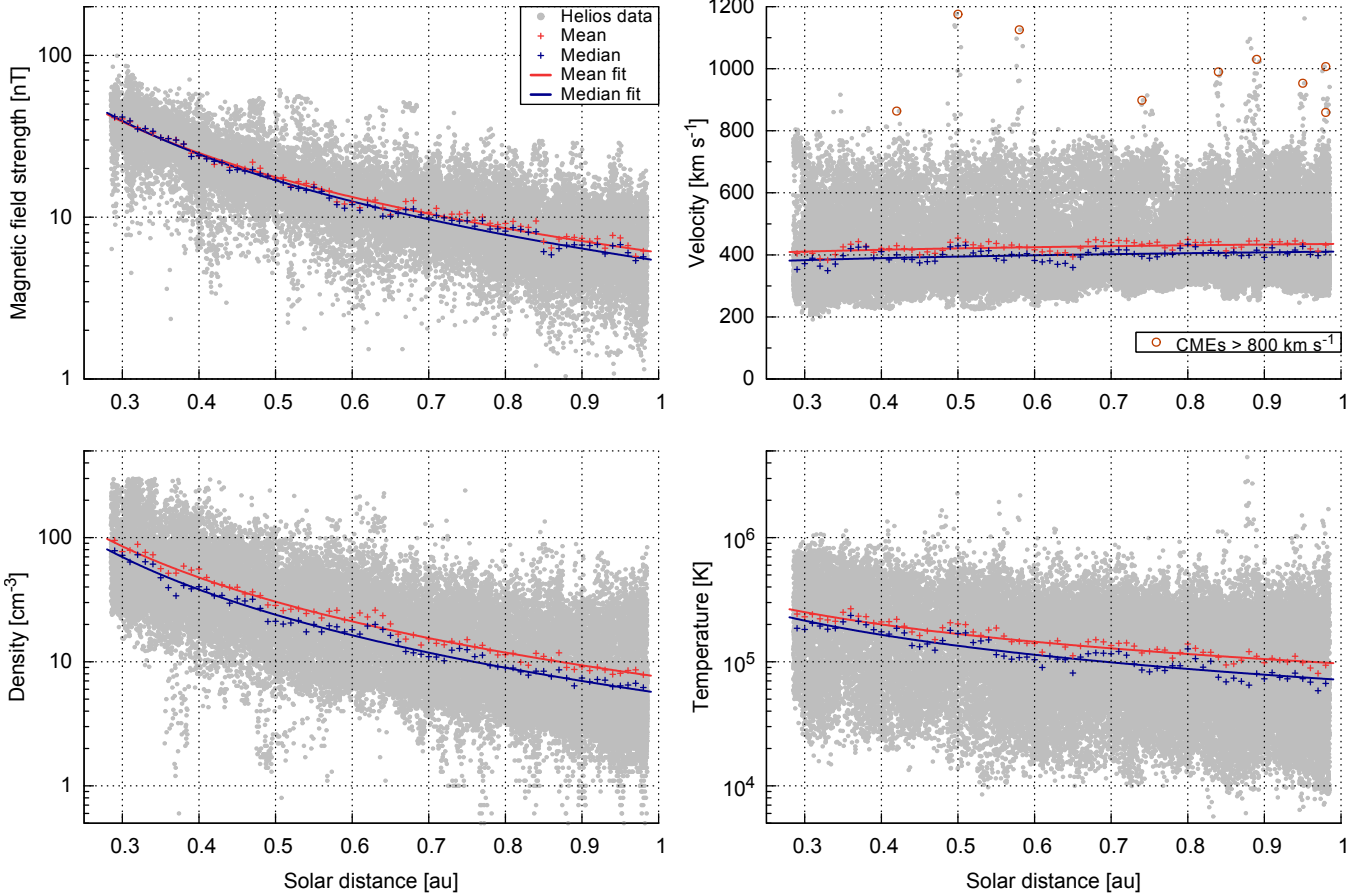


Fig. 7. Helios hourly data plots of the four solar wind parameters over solar distance. The mean and median per 0.01 au data bin and their fit curves are plotted as well. The Helios data has a native distance resolution of 0.01 au, thus, to make the distribution visible in these plots, we added a random distance value of up to ± 0.005 au. The high velocity data points above 800 km s^{-1} (circled red) are identified as CME events (e.g., Sheeley et al. 1985; Bothmer & Schwenn 1996, 1998).

Table 4. Fit coefficients for the distance-dependent single lognormal function, based on Eq. (4) combined with (10) from the combined Helios data.

Parameter	Median d'_{med}	Mean d'_{avg}	Exponent e'	Balance c'	Seasonal variation $\Delta d [\%]$
Magnetic field [nT]	5.358(25)	5.705(28)	-1.662(11)	–	2.8
Density [cm^{-3}]	5.424(33)	6.845(47)	-2.114(20)	–	3.6
Temperature [10^4 K]	6.357(64)	10.72(14)	-1.100(20)	–	1.9
Velocity [10^2 km s^{-1}]	W''_1 3.707(13) W''_2 5.26(13) W''_{II} 4.13(13) ^a	3.748(16) 5.42(11) 4.47(11) ^a	0.0990(51)	0.557(45)	0.17

Notes. Regarding the velocity, the double lognormal function (5) is used instead. The numbers in parentheses are the errors on the corresponding last digits of the quoted value. They are calculated from the estimated standard deviations of the fit parameters. The seasonal variations are calculated from Earth's orbital solar distance variation and the derived exponents. ^(a) Velocity median and mean 1 au values for the resulting function. Error estimates derived from the individual fit part errors.

1 same resolution as for the OMNI data analyzed in Sect. 2 – the
2 distributions and their median values are plotted in Fig. 8. For
3 simplification, as mentioned before, we treat the exponents of
4 the median and mean fit functions as being identical, using one
5 fit parameter for both. Implementing the power law distance de-
6 pendency (10) into the lognormal function (4), we get the fit pa-
7 rameters d'_{med} , d'_{avg} and the common exponent e' . Again, we use
8 the double lognormal function (5) for the velocity distribution
9 fit – resulting in $W''_{\text{II}}(x, r)$. The additional fit parameters are the
10 balancing parameter c' and for the second lognormal part $d'_{\text{med},2}$

and $d'_{\text{avg},2}$. The resulting fit coefficients for the four solar wind
11 parameters are presented in Table 4.

The velocity balancing parameter $c' = 0.557$ is in good
12 agreement with the results for the SSN dependency (9), be-
13 cause with a mean SSN of 59 during the Helios time period,
14 $c(59) = 0.53$, as can be seen from Fig. 6.

The power law lognormal models and the power law dou-
15 ble lognormal model for the velocity, which result from the fit-
16 ting, are plotted in Fig. 8 together with their median values.
17 The model's magnetic field strength is broader around values
18

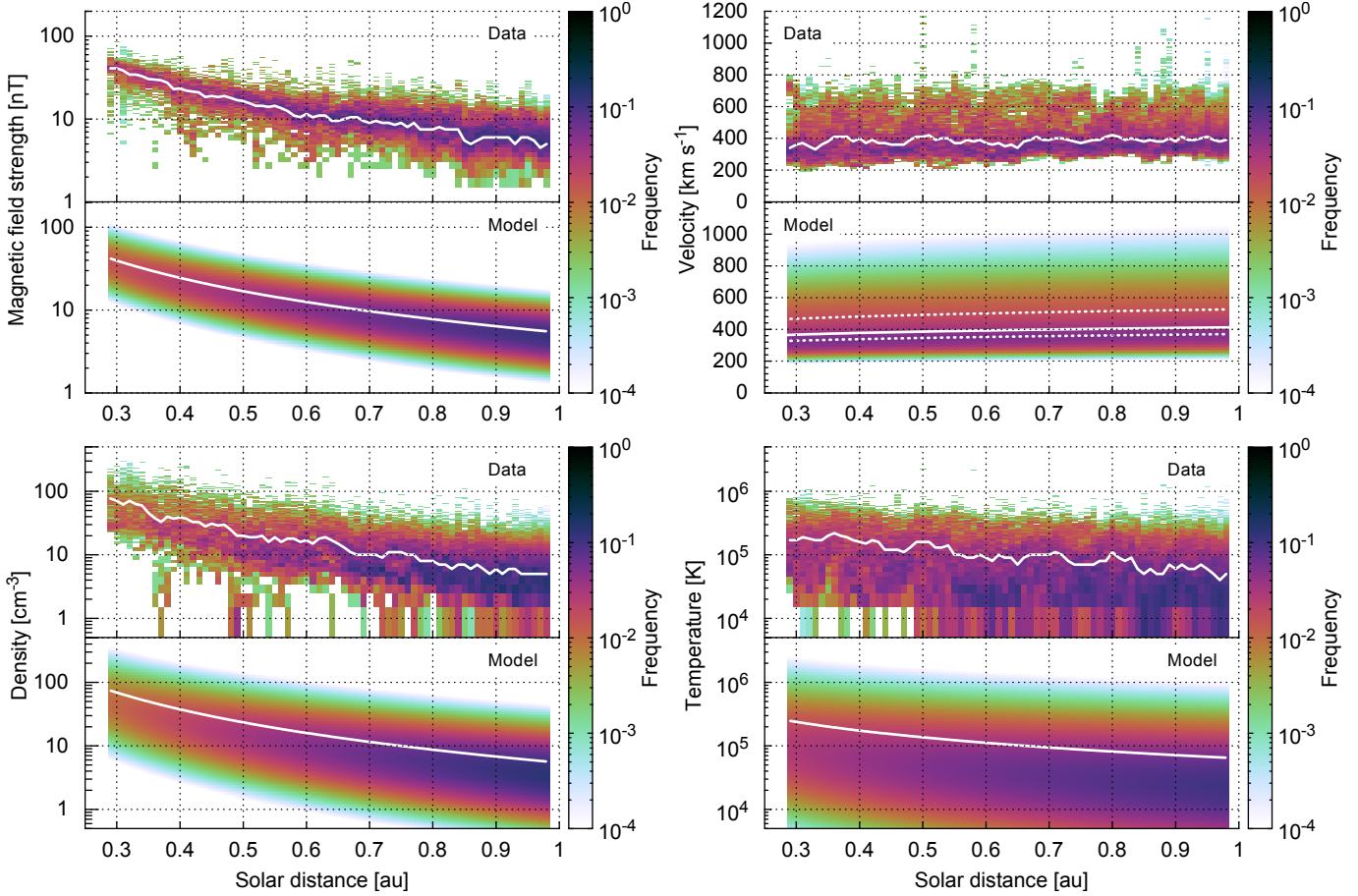


Fig. 8. Frequency distributions of the four solar wind parameters with respect to solar distance. Plotted are the binned Helios data and the power law lognormal fit models with their median values (white lines). The double lognormal model is used for the velocity, its slow and fast parts are indicated by dotted lines.

of 40 nT at the lower distance boundary than the data's frequency distribution implies. This behavior is expected because of the applied distance-independent shape approximation. The velocity and temperature models' upper values generally show a higher abundance than the actual data; see also zoom boxes in Figs. 1 and 2. The high-velocity tail that increases with distance arises from using the same exponent for both slow and fast components. This effect is not seen in the data; more specifically, not only the slowest wind but also the fastest wind is expected to converge to more average speeds (Sanchez-Diaz et al. 2016).

5. Empirical solar-wind model

In order to estimate the solar-wind environment for the PSP orbit, we combine the results from the solar-wind frequency distributions' solar-activity relationships and their distance dependencies derived from the OMNI and Helios data. The result is an empirical solar-wind model for the inner heliosphere which is then extrapolated to the PSP orbit in Sect. 6.

This solar-wind model for the radial distance dependence is representative for the time of the Helios observations around the rise of solar cycle 21. The variations of the yearly power law fit exponents from fitting the solar-distance dependency (10) are shown in Fig. 9 together with the yearly SSN for the time period 1974–1982. It can be seen that during the Helios time period there might be some systematic variation of the exponents with solar activity – at least for the velocity and temperature

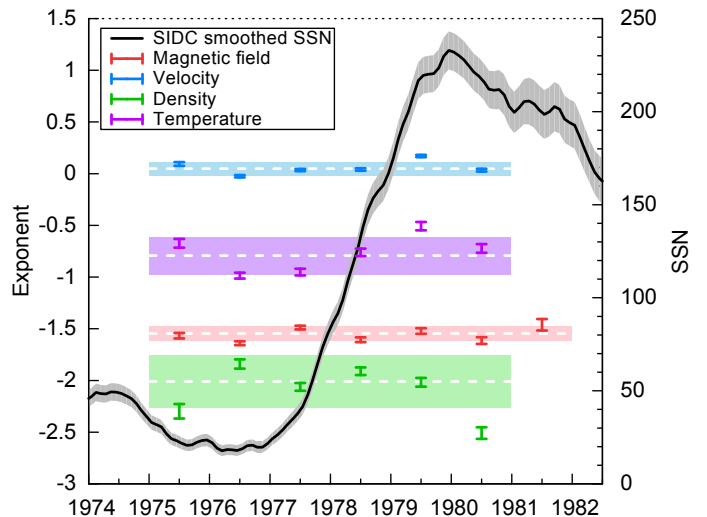


Fig. 9. Helios yearly variation of the solar wind parameter power exponents for the dependence on radial distance together with the SIDC 13-month smoothed monthly SSN. The weighted standard deviations and average values for all years are indicated by the shaded areas. In this plot, the 21 days since Helios launch in the year 1974 are omitted because a distance range of merely 0.95–0.98 au was covered that year.

exponents. However, for simplicity we assume that the distance scaling laws can be treated as time independent and include

1 the calculated exponents' yearly variations Δe , summarized in
 2 Table 3, as relative uncertainties.

3 Since we neglect possible variations of the distance scaling
 4 laws, we combine the frequency distribution's median solar ac-
 5 tivity dependency (7) derived for 1 au from the OMNI data with
 6 the power law exponents (10) derived from the Helios data:

$$x_{\text{med}}(ssn, r) = (a_{\text{med}} \cdot ssn + b_{\text{med}}) \cdot r^{e'}. \quad (11)$$

7 Thus, implementing the median and mean relations into the
 8 lognormal function (4), we obtain the combined model func-
 9 tion $W'''(x, ssn, r)$ and for the velocity $W''''(x, ssn, r)$ with the
 10 double lognormal function (5). The corresponding median and
 11 mean relations for each solar-wind parameter, based on the val-
 12 ues resulting from our analyses, are listed below. Their numeri-
 13 cal values are the fit parameters from Table 2 and the exponents
 14 from Table 4.

- 15 – The magnetic field strength relations, depending on solar ac-
 16 tivity and solar distance, are:

$$B_{\text{med}}(ssn, r) = (0.0131 \text{ nT} \cdot ssn + 4.29 \text{ nT}) \cdot r^{-1.66}, \quad (12)$$

$$B_{\text{avg}}(ssn, r) = 1.0879 \cdot B_{\text{med}}(ssn, r). \quad (13)$$

- 17 – The proton velocity relations for the slow and fast compo-
 18 nents, depending on solar distance, are:

$$v_{\text{med}}^{\text{slow}}(r) = 363 \text{ km s}^{-1} \cdot r^{0.099}, \quad v_{\text{med}}^{\text{fast}}(r) = 483 \text{ km s}^{-1} \cdot r^{0.099}, \quad (14)$$

$$v_{\text{avg}}^{\text{slow}}(r) = 1.0101 \cdot v_{\text{med}}^{\text{slow}}(r), \quad v_{\text{avg}}^{\text{fast}}(r) = 1.023 \cdot v_{\text{med}}^{\text{fast}}(r). \quad (15)$$

19 The share of both components balanced with solar activity is
 20 found to be:

$$c(ssn) = -0.00180 \cdot ssn + 0.64. \quad (16)$$

- 21 – The derived relations of the proton density are:

$$n_{\text{med}}(ssn, r) = (0.0038 \text{ cm}^{-3} \cdot ssn + 4.50 \text{ cm}^{-3}) \cdot r^{-2.11}, \quad (17)$$

$$n_{\text{avg}}(ssn, r) = 1.305 \cdot n_{\text{med}}(ssn, r). \quad (18)$$

- 22 – The derived proton temperature relations are:

$$T_{\text{med}}(ssn, r) = (197 \text{ K} \cdot ssn + 57\,300 \text{ K}) \cdot r^{-1.10}, \quad (19)$$

$$T_{\text{avg}}(ssn, r) = 1.654 \cdot T_{\text{med}}(ssn, r). \quad (20)$$

23 These relations average over seasonal variations because they
 24 are based on yearly data. The OMNI data are time-shifted to the
 25 nose of the Earth's bow shock; this leads to yearly solar distance
 26 variations of $\pm 1.67\%$ as it orbits the Sun. The resulting maxi-
 27 mal solar-wind parameter variation amplitudes over the year can
 28 thus be derived from the derived power law exponents. They are
 29 estimated to be smaller than 4% as seen in Table 4. Bruno et al.
 30 (1986) and Balogh et al. (1999) have pointed out that the solar-
 31 wind parameters vary with latitudinal separation from the helio-
 32 spheric current sheet. Its position in heliographic latitude is
 33 highly variable around the solar equator (Schwenn 1990) and,
 34 furthermore, the Earth's orbit varies over the course of the year
 35 by $\pm 7.2^\circ$ in latitude. Since this latitudinal separation is highly
 36 variable and requires significant effort to calculate for an ex-
 37 tended time series, we have ignored this aspect in this analysis.

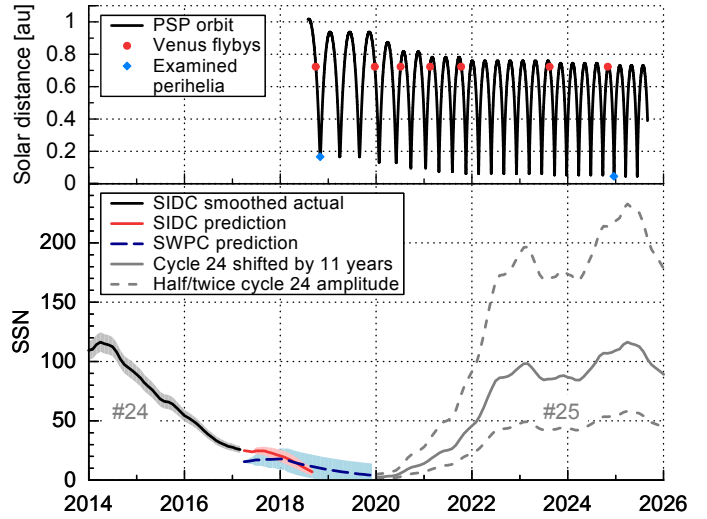


Fig. 10. PSP's solar distance during its mission time (*top*). Consecutive Venus flybys bring its perihelia nearer to the Sun. Actual and predicted SSN (*bottom*), that is, SIDC 13-month smoothed monthly actual SSN, SIDC Standard Curves Kalman filter prediction and SWPC prediction with their corresponding expected ranges (shaded areas). The SSN from previous cycle 24, shifted by 11 yrs, is plotted together with two alternative trends of half and twice its amplitude.

6. Model extrapolation to PSP orbit

To estimate PSP's solar-wind environment during its mission time for its orbital positions, predictions of the SSN during the mission are incorporated into the empirical solar-wind model, derived in the previous sections, and extrapolations down to the PSP perihelion region are performed.

Parker Solar Probe is planned to launch in mid 2018. With its first Venus flyby it will swing into Venus' orbital plane, reaching a first perihelion with a distance of 0.16 au just 93 days after launch, in November 2018. Seven additional Venus flybys allow the perihelion distance to be reduced to a minimum of $9.86 R_\odot$. This distance will be reached with the 22nd perihelion in December 2024 (Fox et al. 2015), as plotted in the top panel of Fig. 10.

We extrapolate the derived empirical solar-wind models to PSP's orbital distance range and compare the results with those from the existing models shown in Fig. 11. The model and its extrapolation are visualized for the SSN range between solar minimum and maximum ($0 \leq ssn \leq 200$), indicated by the shaded regions in the figure. The magnetic field strength is found to increase from median values of about 43 nT at 0.25 au to 715 nT at 0.046 au for a SSN of zero. Taking a SSN of 200 increases the values to 69 nT and 1152 nT. Our extrapolation results are slightly flatter than those derived from the analytical magnetic field model by Banaszkiewicz et al. (1998), who constructed an analytic dipole plus quadrupole plus current sheet (DQCS) model for solar minimum. We note that one cannot easily compare the absolute values of our study with the values obtained by Banaszkiewicz et al. (1998) because the DQCS model assumes solar wind originating from coronal holes at higher heliographic latitudes only, neglecting the slow solar-wind belt. We suggest that the difference in slope is due to the previously mentioned (Sect. 4) changing shape of the frequency distribution with heliocentric distance, which for smaller distances deviates more from the model's lognormal distribution. The average velocity is found to decrease from 340 km s^{-1} at 0.25 au to about 290 km s^{-1} at 0.046 au 3 yrs after a SSN of zero occurred, whereas using a SSN of 200 it decreases from 390 km s^{-1} to 330 km s^{-1} .

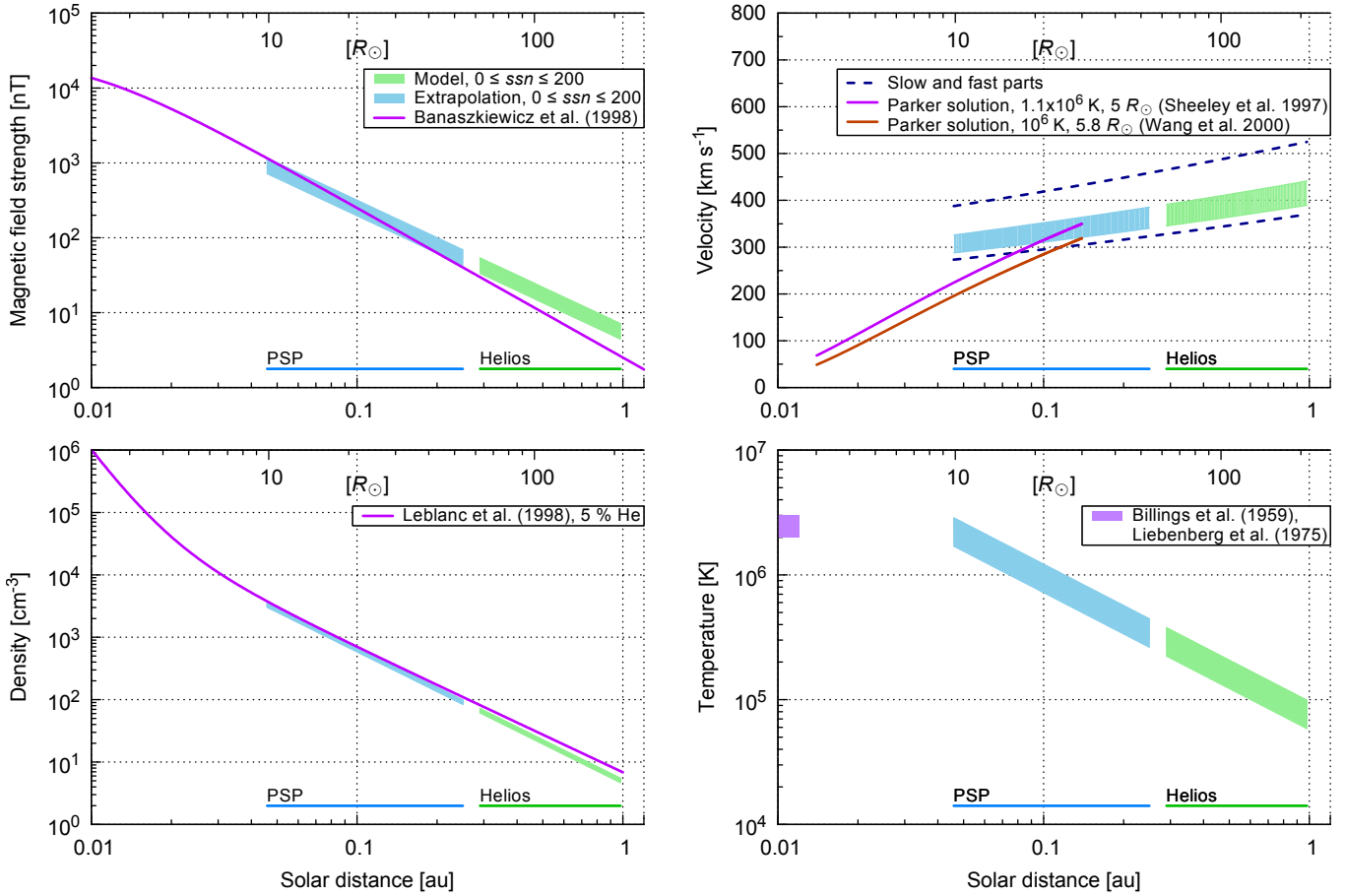


Fig. 11. Radial extrapolation of the solar-wind parameters to the PSP orbit region. The median values from the models, obtained from Helios and OMNI measurements, are extrapolated to the PSP region for SSN values between solar minimum and maximum, that is, $0 \leq \text{ssn} \leq 200$. The lower edges of the shaded areas correspond to solar minimum, the upper edges to solar maximum. Also plotted are the radial dependencies of the analytic DQCS magnetic field model for solar minimum from Banaszkiewicz et al. (1998), the slow wind velocity models from Sheeley et al. (1997) and Wang et al. (2000), the density model from Leblanc et al. (1998) and the range of temperature measurements from Billings (1959) and Liebenberg et al. (1975).

1 Comparing the results with the measurements by Sheeley et al.
2 (1997) and Wang et al. (2000) shows an overestimation in our
3 extrapolated slow solar-wind velocity values for distances below
4 approximately $20 R_\odot$. They used LASCO coronagraph observa-
5 tions to track moving coronal features (blobs) in the distance
6 range $2-30 R_\odot$ to determine speed profiles and sources of the
7 slow solar wind and they derived temperature and sonic point
8 values for slow solar wind with the isothermal expansion model
9 from Parker (1958). Therefore, it generally can be expected that
10 PSP will encounter a slower solar-wind environment close to
11 the Sun than our model estimates. Thus PSP will measure solar-
12 wind acceleration processes (McComas et al. 2008), maybe even
13 still at $30 R_\odot$ as the study by Sheeley et al. (1997) suggests. The
14 proton density increases from about 84 cm^{-3} at 0.25 au to about
15 3018 cm^{-3} at 0.046 au 6 yrs after a SSN of zero occurred. Being
16 almost independent of the SSN, the values for a SSN of 200 are
17 only 17% larger. The results are in good agreement with those
18 of Leblanc et al. (1998), who derived an electron density model
19 from type III radio burst observations. Their model shows that
20 the density distance dependency scales with r^{-2} and steepens just
21 below $10 R_\odot$ with r^{-6} . We assumed a solar-wind helium abun-
22 dance of 5% to convert these electron densities to proton densi-
23 ties. The extrapolated proton temperature increases from about
24 260 000 K at 0.25 au to about 1 690 000 K at 0.046 au 3 yrs af-
25 ter a SSN of zero occurred and from 440 000 K to 2 860 000 K

for a SSN of 200. Knowing that near-Sun coronal temperatures are in the range of 2–3 MK (Billings 1959; Liebenberg et al. 1975), the model overestimates the extrapolated temperatures at the PSP perihelion distance.

Aside from the solar distance, the derived solar-wind parameter models depend on the SSN. Short-term predictions of the SSN can be used for the solar-wind predictions of PSP's early perihelia and also for refining the solar-wind predictions during PSP's mission. Several sources are available for SSN short-term predictions. The SIDC provides 12-month SSN forecasts⁶ obtained from different methods (e.g., Kalman filter Standard Curve method). The SSN prediction of NOAA's Space Weather Prediction Center (SWPC) for the time period until the end of 2019 follows a consensus of the Solar Cycle 24 Prediction Panel⁷. The SSN for PSP's first perihelion will be small – certainly below 20 – whereas the SSN during the closest perihelia, which will commence at the end of 2024 at the likely maximum phase of cycle 25, cannot be predicted at this time. However, Hathaway & Upton (2016) found indications that the next solar cycle will be similar in size to the current cycle 24. Therefore we simply assume a pattern similar to the last cycle

⁶ <http://sidc.be/silso/forecasts>

⁷ <http://www.swpc.noaa.gov/products/solar-cycle-progression>

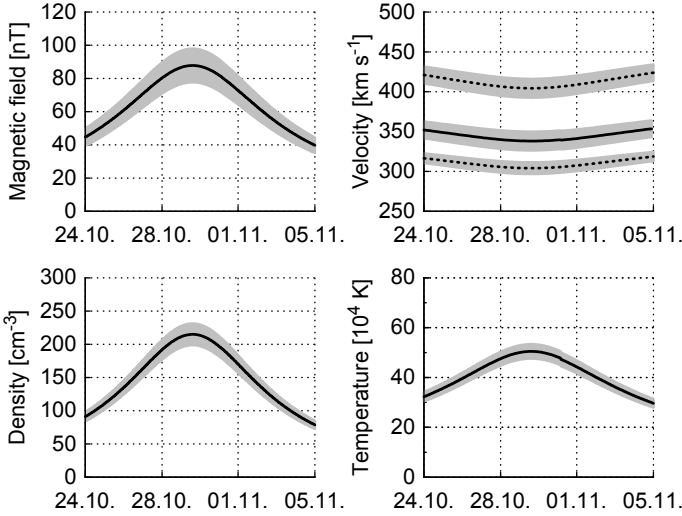


Fig. 12. Estimated solar-wind parameter medians (black lines) and their error bands (gray) during 12 days in 2018 with PSP's first perihelion at about 0.16 au. For the velocity the combined median is calculated and also the SSN-independent slow and fast parts are plotted (dotted lines).

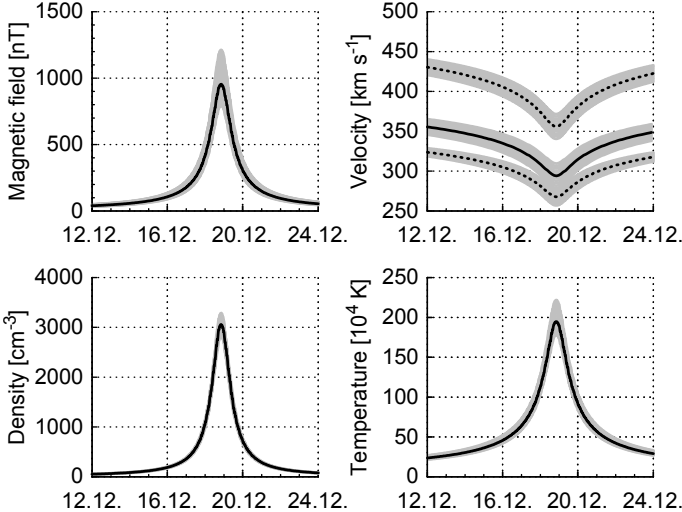


Fig. 13. Estimated solar-wind parameter medians (black lines) and their error bands (gray) during 12 days in 2024 with PSP's 22nd (the first closest) perihelion at 0.0459 au. For the velocity the combined median is calculated and also the SSN-independent slow and fast parts are plotted (dotted lines).

for the prediction of the next solar cycle and thus shift the last cycle by 11 yrs. Additionally, we consider as possible alternatives SSN patterns of half and twice its amplitude as shown in the bottom panel of Fig. 10.

Implementing the SSN predictions for the PSP mission time and the orbital trajectory data, we can infer which solar-wind parameter magnitudes can be expected. Figures 12 and 13 show the median values (7) of the considered different solar-wind parameters for 12-day periods, comprising the first perihelion in November 2018 and the first closest perihelion in December 2024. In the beginning of the mission median values of about 87 nT, 340 km s⁻¹, 214 cm⁻³ and 503 000 K are estimated to be measured at 0.16 au, increasing to about 943 nT, 290 km s⁻¹, 2951 cm⁻³ and 1 930 000 K during the first closest approach at 0.046 au. Monthly SSNs – shifted by the time lags specific to the solar-wind parameters – are used in the calculation of the solar-wind predictions. These SSNs are either actual

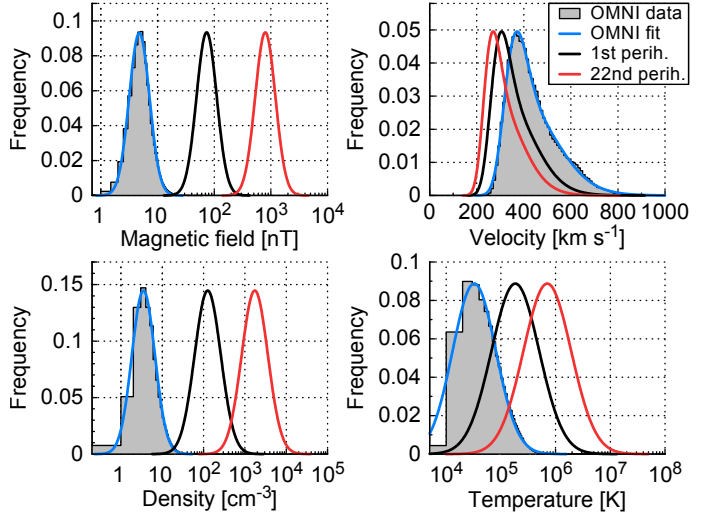


Fig. 14. Frequency distributions of the four solar-wind parameters (same as in Figs. 1 and 2) and those estimated with the solar-wind model for PSP's 1st and 22nd (first closest) perihelion. In these figures the frequencies of both extrapolated curves are scaled for visibility to the same height as the 1 au distribution.

smoothed values from the SIDC with their reported standard deviations, short-term predictions from the SWPC with their expected ranges, or actual smoothed values from the SIDC shifted by 11 yrs with half/twice their values as uncertainties. The error bands given in both figures, calculated from error propagation, include these SSN ranges and the derived fit parameter errors.

Finally the estimated solar-wind environment can be derived from the function $W'''(x, ssn, r)$. The estimated frequency distributions of the four solar-wind parameters at PSP's 1st and 22nd (first closest) perihelion are plotted in Fig. 14. Again, we point out that the velocity and temperature distributions for the 22nd perihelion are only upper limits and the actual values to be encountered by PSP are expected to be smaller.

7. Discussion and summary

The scientific objective of this study, being part of the CGAUSS project – the German contribution to the WISPR instrument – is to model the solar-wind environment for the PSP mission to be launched mid 2018. For this purpose we started the development of the empirical solar-wind environment model for the near-ecliptic PSP orbit. We derived lognormal representations of the in situ near-Earth solar-wind data collected in the OMNI database, using the frequency distributions of the key solar-wind parameters, magnetic field strength, proton velocity, density, and temperature. Throughout the different analyses in our study, the velocity's frequency distribution is treated as a composition of a slow and a fast wind distribution. Each velocity part is fitted with a lognormal function, which allows for the overlap of both velocity ranges. The OMNI multi-spacecraft solar-wind data is intercalibrated and covers almost five solar cycles. It thus represents solar wind gathered at different phases of solar activity in the ecliptic plane. In the next step we investigated the yearly variation of the solar-wind distribution functions along with the SSN over 53 yrs and derived linear dependencies of the solar-wind parameters with the SSN. The radial dependencies of the solar-wind distribution functions were then analyzed, using Helios 1 and 2 data for the distance range 0.29–0.98 au in bins of 0.01 au, deriving power law fit functions that were used to scale the previously calculated SSN-dependent 1 au distribution

1 fit functions to the PSP orbit, taking into account SSN predictions
 2 for the years 2018–2025, encompassing the prime mission
 3 up to the closest approach of $9.86 R_{\odot}$. The reason for performing
 4 the analysis this way is based on the fact that the OMNI solar-
 5 wind database is much larger than the Helios database.

6 For determining solar-activity- and solar-distance-dependent
 7 relations for the median and mean solar-wind values, we could
 8 have used the simpler approach of combining the radial dependence
 9 of averaged Helios data with averaged 1 au OMNI data
 10 scaled with the SSN. It is expected that the results of a simpler
 11 analysis would have similar distance scaling results, as can be
 12 inferred from the exponents in Tables 3 and 4. However, in our
 13 study we are not only interested in averages but rather in bulk
 14 distributions, that is, the whole range of values that might occur.
 15 For the determination of the frequency distributions the use of
 16 the more complex fit model is important, because the distance
 17 between median and mean values determines the width of the
 18 lognormal distributions.

19 It is clear that the calculated distribution functions only rep-
 20 resent first-order estimates of the real solar wind to be encoun-
 21 tered by PSP. The solar-wind environment to be encountered
 22 will depend at times of PSP on the structure of the solar corona
 23 and underlying photospheric magnetic field and on the evolu-
 24 tion and interaction of individual solar-wind streams and super-
 25 imposed CMEs and shocks. However, the derived results are in
 26 good agreement with existing studies about near-Sun solar-wind
 27 magnetic field strengths and densities as shown in Sect. 6. The
 28 extrapolation results of the velocity and the temperature differ
 29 from the direct measurements seen in existing studies. This sug-
 30 gests that below about $20 R_{\odot}$ PSP may dive into the region where
 31 the acceleration and heating of the solar wind is expected to oc-
 32 cur (see Fig. 11). The near-Sun solar-wind velocity at PSP per-
 33 helion is also expected to be slower than our model estimates,
 34 because the solar wind is assumed to be accelerated up to the
 35 height of the Alfvénic critical surface, which is predicted to
 36 lie on average around $17 R_{\odot}$ (e.g., Sittler & Guhathakurta 1999;
 37 Exarhos & Moussas 2000), scaling with solar activity within a
 38 range of between $15 R_{\odot}$ at solar minimum and $30 R_{\odot}$ at solar
 39 maximum (Katsikas et al. 2010; Goelzer et al. 2014).

40 We have not specifically investigated the occurrences of ex-
 41 treme solar-wind parameters caused by CMEs or enhanced val-
 42 ues due to stream interaction or co-rotating interaction regions.
 43 The Helios solar-wind measurements plotted over radial distance
 44 in Fig. 7 show several extreme values far above the usual solar-
 45 wind velocities, which are associated with individual CMEs. The
 46 results by Sachdeva et al. (2017) indicate that due to solar-wind
 47 drag, the speeds of fast CMEs will commonly slow down sub-
 48 stantially from early distances of a few solar radii. Therefore,
 49 it is expected that PSP will encounter CMEs with much higher
 50 speeds than those observed during the Helios mission. Also, the
 51 magnetic field, density and temperature values are expected to
 52 be much larger than in the average solar wind in individual fast-
 53 shock-associated CME events. PSP will thus also substantially
 54 improve our understanding of the near-Sun evolution of CMEs
 55 and their expansion with radial distance.

56 With the resulting CGAUSS empirical solar-wind model for
 57 PSP, the following main results for the bulk solar-wind parame-
 58 ters and estimations for their median values at PSP’s first peri-
 59 helion in 2018 at a solar distance of 0.16 au and at PSP’s closest
 60 perihelia beginning in 2024 at 0.046 au ($9.86 R_{\odot}$) are obtained:

- 61 – The dependency of the magnetic field strength on solar ac-
 62 tivity and radial distance appears to be valid above $20 R_{\odot}$,

however near PSP’s closest perihelia, the actual values might
 be found to be slightly higher.

- The estimated magnetic field strength median values ob-
 tained from relation (12) for PSP’s 1st and 22nd perihelion are 87 nT and 943 nT.
- The radial dependencies of the proton velocity median val-
 ues for slow and fast solar wind (14) appear to be valid
 above about $20 R_{\odot}$ solar distance; below they overestimate
 the actual solar wind velocities obtained from remote mea-
 surements. The share of their frequency distributions to the
 overall solar-wind velocity distribution (5) depends on solar
 activity with their balance relation (16). Thus, at solar mini-
 mum, with a SSN of around zero, the slow-wind component
 contributes about 64% and drops to 28% during solar maxi-
 mum conditions with a SSN around 200.
- The calculated median velocity values for PSP’s 1st and
 22nd perihelion are 340 km s^{-1} and 290 km s^{-1} .
- The proton density relation appears to be valid throughout
 the full PSP orbital distance range, even down to about $8 R_{\odot}$.
- The estimated density median values obtained from relation
 (17) for PSP’s 1st and 22nd perihelion are 214 cm^{-3} and
 2951 cm^{-3} .
- The derived correlation function for the proton tempera-
 ture appears to provide overly high temperature values
 around PSP’s closest perihelion in comparison to coronal
 measurements.
- The estimated temperature median values obtained from re-
 lation (19) for PSP’s 1st and 22nd perihelion are 503 000 K
 and 1 930 000 K.

The results of the modeled solar-wind environment will be use-
 ful to help optimize the WISPR and in situ instrument science
 plannings and PSP mission operations. This also applies for the
 Heliospheric Imager (SoloHI; Howard et al. 2013) and the in situ
 instruments on board the Solar Orbiter spacecraft.

Acknowledgements. The authors acknowledge support of the Coronagraphic German and US SolarProbePlus Survey (CGAUSS) project for WISPR by the German Aerospace Center (DLR) under grant 50 OL 1601 as national contribution to the Parker Solar Probe mission. The authors thank the Helios and OMNI PIs/teams for creating and making available the solar wind in situ data. The Helios and the OMNI data are supplied by the NASA Space Science Data Coordinated Archive and the Space Physics Data Facility at NASA’s Goddard Space Flight Center. Additional thanks for maintaining and providing the international sunspot number series goes to the World Data Center – Sunspot Index and Long-term Solar Observations at the Solar Influences Data Analysis Center, Royal Observatory of Belgium. The PSP SPICE kernel was kindly provided by Angelos Vourlidas. The authors thank the referee for the careful review of this manuscript and helpful comments and suggestions.

References

- Bale, S. D., Goetz, K., Harvey, P. R., et al. 2016, *Space Sci. Rev.*, 204, 49
 Balogh, A., Bothmer, V., Crooker, N. U., et al. 1999, *Space Sci. Rev.*, 89, 141
 Banaszkiewicz, M., Axford, W. I., & McKenzie, J. F. 1998, *A&A*, 337, 940
 Belcher, J. W., Slavin, J. A., Armstrong, T. P., et al. 1991, *Mercury Orbiter: Report of the Science Working Team* (Washington, United States)
 Biermann, L. 1951, *ZAp*, 29, 274
 Billings, D. E. 1959, *ApJ*, 130, 961
 Bothmer, V., & Daglis, I. A. 2007, *Space Weather – Physics and Effects* (Praxis Publishing)
 Bothmer, V., & Schwenn, R. 1996, *Adv. Space Res.*, 17
 Bothmer, V., & Schwenn, R. 1998, *Annales Geophysicae*, 16, 1
 Bougeret, J.-L., King, J. H., & Schwenn, R. 1984, *Sol. Phys.*, 90, 401
 Bruno, R., Villante, U., Bavassano, B., Schwenn, R., & Mariani, F. 1986, *Sol. Phys.*, 104, 431
 Burt, J., & Smith, B. 2012, in 2012 IEEE Aerospace Conference, 1
 Colin, L. 1980, *J. Geophys. Res.*, 85, 7575

1 Domingo, V., Fleck, B., & Poland, A. I. 1995, *Sol. Phys.*, 162, 1
 2 Exarhos, G., & Moussas, X. 2000, *A&A*, 356, 315
 3 Feldman, W. C., Asbridge, J. R., Bame, S. J., & Gosling, J. T. 1978,
 J. Geophys. Res., 83, 2177
 4 Forsyth, R. J., Bothmer, V., Cid, C., et al. 2006, *Space Sci. Rev.*, 123, 383
 5 Fox, N. J., Velli, M. C., Bale, S. D., et al. 2015, *Space Sci. Rev.*
 6 Goelzer, M. L., Schwadron, N. A., & Smith, C. W. 2014, *J. Geophys. Res. (Space
 Phys.)*, 119, 115
 7 Gosling, J. T., Hildner, E., MacQueen, R. M., et al. 1974, *J. Geophys. Res.*, 79,
 4581
 8 Gringauz, K. I., Bezrukikh, V. V., Ozerov, V. D., & Rybchinskii, R. E. 1960,
 Soviet Physics Doklady, 5, 361
 9 Gurnett, D. A., Kurth, W. S., Burlaga, L. F., & Ness, N. F. 2013, *Science*, 341,
 1489
 10 Hathaway, D. H., & Upton, L. A. 2016, *J. Geophys. Res. (Space Phys.)*, 121,
 10
 11 Hellinger, P., Matteini, L., Šverák, Š., Trávníček, P. M., & Marsch, E. 2011, *J.
 Geophys. Res. (Space Phys.)*, 116, A09105
 12 Hellinger, P., Trávníček, P. M., Šverák, Š., Matteini, L., & Velli, M. 2013, *J.
 Geophys. Res. (Space Phys.)*, 118, 1351
 13 Howard, R. A., Vourlidas, A., Korendyke, C. M., et al. 2013, in *Solar Physics
 and Space Weather Instrumentation V*, Proc. SPIE, 8862, 88620
 14 Kasper, J. C., Stevens, M. L., Korreck, K. E., et al. 2012, *ApJ*, 745, 162
 15 Kasper, J. C., Abiad, R., Austin, G., et al. 2016, *Space Sci. Rev.*, 204, 131
 16 Katsikas, V., Exarhos, G., & Moussas, X. 2010, *Adv. Space Res.*, 46, 382
 17 Kilpua, E. K. J., Madjarska, M. S., Karna, N., et al. 2016, *Sol. Phys.*, 291, 2441
 18 King, J. H., & Papitashvili, N. E. 2005, *J. Geophys. Res. (Space Phys.)*, 110,
 A02104
 19 Lazarus, A. J. 2000, *Science*, 287, 2172
 20 Leblanc, Y., Dulk, G. A., & Bougeret, J.-L. 1998, *Sol. Phys.*, 183, 165
 21 Lepping, R. P., Acuña, M. H., Burlaga, L. F., et al. 1995, *Space Sci. Rev.*, 71, 207
 22 Liebenberg, D. H., Bessey, R. J., & Watson, B. 1975, *Sol. Phys.*, 44, 345
 23 Mariani, F., Ness, N. F., Burlaga, L. F., Bavassano, B., & Villante, U. 1978,
 J. Geophys. Res., 83, 5161
 24 McComas, D. J., Bame, S. J., Barracough, B. L., et al. 1998, *Geophys. Res. Lett.*,
 25, 1
 25 McComas, D. J., Acton, L. W., Balat-Pichelin, M., et al. 2008, *Solar Probe
 Plus: Report of the Science and Technology Definition Team*, Tech. Rep.
 NASA/TM-2008-214161, National Aeronautics and Space Administration,
 Goddard Space Flight Center, Greenbelt, MD
 26 McComas, D. J., Alexander, N., Angold, N., et al. 2016, *Space Sci. Rev.*, 204,
 187
 27 McGregor, S. L., Hughes, W. J., Arge, C. N., Odstrcil, D., & Schwadron, N. A.
 2011a, *J. Geophys. Res. (Space Phys.)*, 116, A03106
 28 McGregor, S. L., Hughes, W. J., Arge, C. N., Owens, M. J., & Odstrcil, D. 2011b,
 J. Geophys. Res. (Space Phys.), 116, A03101
 29 Müller, D., Marsden, R. G., St. Cyr, O. C., & Gilbert, H. R. 2013, *Sol. Phys.*,
 285, 25
 30 Neugebauer, M., & Snyder, C. W. 1966, *J. Geophys. Res.*, 71, 4469
 31 Ogilvie, K. W., Chornay, D. J., Fritzenreiter, R. J., et al. 1995, *Space Sci. Rev.*,
 71, 55
 32 Parker, E. N. 1958, *ApJ*, 128, 664
 33 Richardson, I. G., & Cane, H. V. 2012, *J. Space Weather and Space Climate*, 2,
 A2
 34 Rosenbauer, H., Schwenn, R., Marsch, E., et al. 1977, *J. Geophysics Zeitschrift
 Geophysik*, 42, 561
 35 Russell, C. T., Mewaldt, R. A., Luhmann, J. G., et al. 2013, *ApJ*, 770, 38
 36 Sachdeva, N., Subramanian, P., Vourlidas, A., & Bothmer, V. 2017, *Sol. Phys.*,
 292, 118
 37 Sanchez-Diaz, E., Rouillard, A. P., Lavraud, B., et al. 2016, *J. Geophys. Res.
 (Space Phys.)*, 121, 2830
 38 Schwenn, R. 1983, in *NASA Conference Publication*, 228
 39 Schwenn, R. 1990, *Large-Scale Structure of the Interplanetary Medium*, eds. R.
 Schwenn, & E. Marsch (Berlin, Heidelberg: Springer), 99
 40 Sheeley, Jr., N. R., Howard, R. A., Michels, D. J., et al. 1985, *J. Geophys. Res.*,
 90, 163
 41 Sheeley, N. R., Wang, Y.-M., Hawley, S. H., et al. 1997, *ApJ*, 484, 472
 42 SILSO World Data Center 1963–2016, *International Sunspot Number Monthly
 Bulletin* and online catalogue
 43 Sittler, Jr., E. C., & Guhathakurta, M. 1999, *ApJ*, 523, 812
 44 Smith, E. J., & Balogh, A. 2003, in *Solar Wind Ten*, eds. M. Velli, R. Bruno,
 F. Malaia, & B. Bucci, AIP Conf. Ser., 679, 67
 45 Stone, E. C., Frandsen, A. M., Mewaldt, R. A., et al. 1998, *Space Sci. Rev.*, 86,
 1
 46 Veselovsky, I. S., Dmitriev, A. V., & Suvorova, A. V. 2010, *Cosmic Research*,
 48, 113
 47 Vourlidas, A., Howard, R. A., Plunkett, S. P., et al. 2016, *Space Sci. Rev.*, 204,
 83
 48 Wang, Y.-M., Sheeley, N. R., Socker, D. G., Howard, R. A., & Rich, N. B. 2000,
 J. Geophys. Res., 105, 25133
 49
 50
 51
 52
 53
 54
 55
 56
 57
 58
 59
 60
 61
 62
 63
 64
 65
 66
 67
 68
 69
 70
 71
 72
 73
 74
 75
 76
 77
 78
 79
 80